M. Quadrio, C. Pipolo, S. Corti, F. Messina, C. Pesci, A.M. Saibene, S. Zampini, G. Felisati
Effects of CT Resolution and Radiodensity Threshold on the CFD Evaluation of Nasal Airflow
Medical & Biological Engineering & Computing, Vol. 54, N. 2, 2016, p. 411-419
doi:10.1007/s11517-015-1325-4

Med Biol Eng Comput manuscript No.
(will be inserted by the editor)

Effects of CT resolution and radiodensity threshold on the CFD evaluation of nasal airflow

Maurizio Quadrio · Carlotta Pipolo · Stefano Corti · Francesco Messina · Chiara Pesci · Alberto M. Saibene · Samuele Zampini · Giovanni Felisati

Received: Accepted: date

Abstract The robustness of a CFD-based procedure for the quantitative evaluation of the nasal airflow is addressed. For CFD to seriously enter the clinical practice, its ability to yield robust results with respect to the unavoidable procedural and modeling inaccuracies must be demonstrated. Here we consider in particular the sensitivity of the CFD procedure to the spatial resolution of the available CT scan, as well as to the choice of the segmentation level of the CT images. It is found that none of the issues presents critical problems, although the choice of the segmentation level is potentially delicate if carried out by a non-expert operator.

Keywords Nasal Cavities · Fluid Dynamics · Computer Simulation

1 Introduction

The wide incidence of nasal breathing difficulties (NBD) is well assessed [17], and in recent years functional endoscopic sinus surgery (FESS) has emerged as the preferred approach for the treatment of chronic NBD. The minimally-invasive FESS is carried out through endoscopic techniques, and may involve inferior and/or middle turbinoplasty, and opening of the paranasal sinuses, depending upon the patient's anatomy and the surgeon's judgment. FESS, often coupled with septoplasty, is aimed to re-establish adequate nasal aerial flow, to increase sinus ventilation, and to improve sinus draining [9].

M. Quadrio · C. Pesci · S. Corti · S. Zampini
Politecnico Milano, Dept. Aerospace Science and Technologies
Via La Masa 34, 20156 Milan, Italy
E-mail: maurizio.quadrio@polimi.it

C. Pipolo · F. Messina · A.M. Saibene · G. Felisati
Otorhinolaryngology Unit, Head and Neck Department, San Paolo Hospital, Università degli Studi di Milano
Via di Rudinì 8, 20142 Milan, Italy

However, assessing the relevance of a single anatomic anomaly (and, as a consequence, the importance of its surgical modification) on the overall nasal flow quality is still a daunting task. Patient history and clinical examination are the obvious starting points, but both are subjective to some degree. Moreover, septal deviation and other anatomical alterations commonly occur in the population but often do not correspond to functional alterations, such that a causal link between the apparent status of the nose and the disruption of its physiological function is not always available. For example the subjective sensation of good nasal airflow, the so-called nasal patency, is of great importance to patients with NBD, but often bears little relationship to the actual physical aerodynamic resistance or drag experienced by the airflow in the nose [12,21]. Furthermore, surgical procedures are typically carried out according to the surgeon's own experience. As a consequence, rationally and reliably predicting the overall effect of any single surgical maneuver on the whole nasal flow is essentially impossible. Even the consequences of a given surgery-induced modification of the inner-nose geometry upon the local airflow quality cannot be fully predicted; the same holds true for its effects on humidification, possible crusting, bleeding, etc.

Our limited understanding of the details of the flow field is partly due to the lack of proper diagnostics. In the past, cadaver noses or models reconstructed from CT and MRI images have been used to understand the general characteristics of nasal airflow [1]. Such models, however, were inconvenient or inaccurate [6], and are obviously of limited help in a patient-specific approach. Rhinomanometry is the only exam that, with a relative accuracy, can evaluate the nasal aerial patency as a function of overall pressure/flow rate [16]. However, rhinomanometry cannot observe any detail of the flow (e.g. specifically in the crucial region of the inferior and middle meati) and only provides us with an as-

sessment of a global measure that indeed descends from a very complex fluid dynamical pattern.

Recently, progresses in modern computational fluid dynamics (CFD) and computer technology are beginning to improve the picture. The Navier–Stokes partial differential equations that govern the dynamics of fluids flowing in complex geometries have become solvable numerically, most typically within the Reynolds-average framework (RANS). In the RANS approach, the governing equations are first averaged in time, so that temporal and small-scale spatial turbulent fluctuations are averaged out, and then numerically solved to obtain the time-mean flow. However, the time-mean effect of the velocity fluctuations upon the mean flow is of paramount importance and must be properly modeled within the RANS approach: this is accomplished through one of the many available so-called turbulence models [13]. After the pionieristic work by [4], who built an extremely simplified model for the nasal cavities and investigated the flow field computationally, early CFD attempts to address the trans-nasal aerodynamics by using various CT-generated three-dimensional geometries, e.g. [10], were based on low-fidelity flow models, and did not reach beyond a qualitative description of the salient global features of the flow. With the passing years, the quality of the numerical prediction has steadily improved, until, very recently, CFD has been proposed [20,2,15,24] as a viable tool to support patient-specific pre-surgical planning, to eventually arrive at what may be called virtual surgery. Several open problems, however, render the daily use of such tools in the clinical practice still quite far from reality. For example, [15] notice how the operator time required to carry out the entire computational procedure is perhaps affordable at research level, but still highly unrealistic in daily clinical use. A recent review can be found in [14], where the main challenges to be addressed before CFD can become of clinical use are identified and critically discussed.

The present paper describes one step towards our long-term goal of designing the best (to be intended at the same time as the least invasive and the most effective) surgical modification on a patient-specific basis, by taking advantage of modern CFD analysis applied to a CT scan. The many outstanding difficulties involved in such a procedure (especially when the reliability of all the computed flow details is requested, instead of a simple global validation of the outcome of the simulation) imply that a close scrutiny of the mathematical models employed in the simulation is in order. The present paper addresses two preliminary, but still essential aspects of the procedure: i) How the end results are affected by the segmentation threshold used to convert the CT images into a three-dimensional computational volume mesh; and ii) How the end results are affected by the quality (spatial resolution) of the CT scan. In other words, we want to check on these prerequisites in order to preliminarily assess the viability for a CFD-based procedure to be widely deployed in clinical use. Such a preliminary feasibility study is motivated by our firm belief that a procedure requiring *ad-hoc* imaging or unsustainable amount of operator time will never attract a large interest for clinical use. The aforementioned checks will be carried out within the framework of basic mathematical flow models, by considering either an unsteady laminar flow in the nasal cavity, or a turbulent flow through a standard turbulence model. Discussion of the best mathematical (turbulence) model and of the criteria for its choice, as discussed for example in [22,8,7] is ongoing work, and is left out of the scope of the present paper.

2 Methods

After approval of the ethics board, one male, 67 years old patient, affected by typical NBD was selected, and a visual analysis of the CT scan confirmed that his anatomic anomalies were within the range of the daily experience of the ENT group. The CT scan was already available, being routinely acquired for such patients, and had a spatial resolution of 512×512 pixel per image (amounting to 0.49×0.49 mm) in the sagittal-coronal plane, and 0.625mm in the axial direction. We asked the radiologists to carry out in this particular case an additional reconstruction at 1.25mm of axial resolution, thus discarding every second plane.

The images from the CT scan were first manipulated with the open-source software 3D-Slicer [5]. 3D-Slicer is a software platform for the analysis (including registration and interactive segmentation) and visualization (including volume rendering) of medical images and for research in image-guided therapy, and was adopted as the software of choice also because it's free, open-source and available on multiple operating systems. 3D-Slicer is used to convert the CT images into an accurate geometrical description of the boundary of the volume of interest, through image segmentation and volume reconstruction. The reconstructed three-dimensional geometry is represented via a STereoLithography (STL) file. This part of our procedure, that precedes the creation of the actual computational mesh where the differential equations of motion are discretized and solved, requires approximately 15–30 minutes of operator time.

The reconstructed geometry is used as an input for the subsequent analysis, by first generating the computational mesh to be used by the CFD software. As CFD tool we employ the open-source CFD package OpenFOAM, which is based upon the work of Weller et al. [19]. Strictly speaking, OpenFOAM is a general C++ library, based on finite-volumes discretization, that allows building solvers for Partial Differential Equations. The package contains what is required to convert the STL geometry into a computational mesh: the tool is called `snappyhexmesh`. It preliminarily

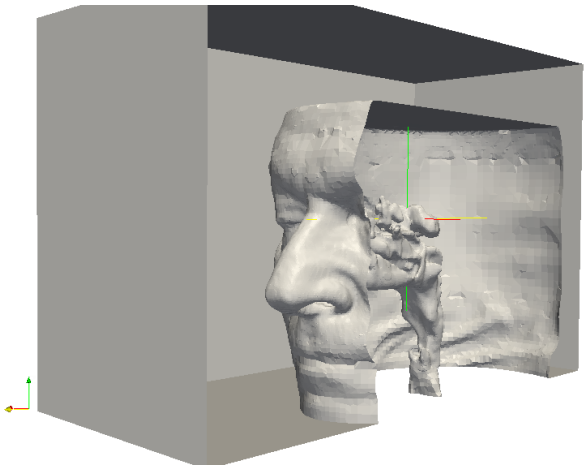

Fig. 1 Three-dimensional view of the surface described by the STL file after the segmentation process. The nasal passageways and the large volume occupied by the nasal sinuses are evident, as well as the patient's face.

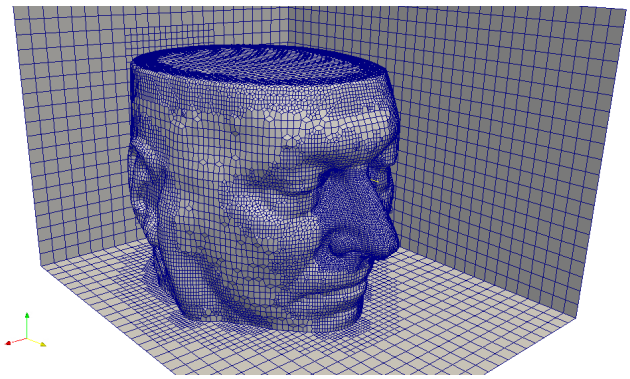

Fig. 2 Three-dimensional view of the computational domain (external part). The gridded volume is the whole air-filled volume, i.e. the portion surrounding the patient's head and delimited by the outer cube, plus the the volume occupied by the nasal passageways down to the nasopharinx and throat. The surface-plotted grid gives a feeling of the spatial resolution employed in the internal volumes.

fills with hexaedrals (castellated mesh) the whole volume of interest, delimited by the reconstructed boundary; in a second step, the castellated mesh is deformed to snap onto the actual boundary; lastly, additional layers of cells may be added near the solid boundaries of the volume of interest, to better cope with the flow boundary layers which develop along the geometric boundaries where the flow velocity obeys the no-slip condition.

The last step is the actual execution of the flow solver, which computes results like velocity, vorticity and pressure fields. The OpenFOAM package contains a number of specialized flow solvers. In the present work, we employ a standard solver for the unsteady incompressible Reynolds-averaged Navies–Stokes equations, with either laminar flow or a turbulence model adopted for their closure. The equations of motions are thus:

$$\nabla \cdot \overline{\mathbf{u}} = 0 \tag{1}$$

$$\frac{\partial \overline{\mathbf{u}}}{\partial t} + \nabla \cdot \left(\overline{\mathbf{u}}\,\overline{\mathbf{u}} + \overline{\mathbf{u}'\mathbf{u}'} \right) + \frac{1}{\rho} \nabla \overline{p} = \nabla^2 \overline{\mathbf{u}} \tag{2}$$

where $\overline{\mathbf{u}}$ is the velocity vector averaged in time (on a time scale shorter that a typical flow timescale), $\mathbf{u}'$ its fluctuations around that mean, and $\overline{p}$ the mean pressure.

Boundary conditions for the differential system (1)–(2) need to be specified. The reconstructed surface of the nasal passageways is considered as a solid wall, where no-slip and no-penetration boundary conditions are applied, i.e. $\overline{\mathbf{u}} = 0$. The two extrema of the actual volume of interest for nasal aerodynamics are the nostrils, representing the inlet side of the boundary for an inspiration, and the nasopharynx region at the outlet boundary. In many of the existing studies, velocity is considered as known and enforced with a Dirichlet-type boundary condition at the inflow; a condition of zero gradient is selected for the velocity vector at the outflow. Since the boundary condition enforced at the inflow turns out to be potentially critical in determining the quality of the final solution, given its proximity to the very important area of the nasal valve, following [3] we also compute the flow field in an additional region made by a box, with dimensions 240 $\times$ 300 $\times$ 200 mm, that surrounds the whole head of the patient. The flow is thus driven by an assigned pressure difference $\Delta\overline{p}$ between the outer surface of the box and the region of the throat. A zero-gradient condition at the inflow is enforced on the velocity components at the faces of the box, thus allowing the full velocity field at the nostrils to be reliably computed as part of the solution process instead of being arbitrarily assigned.

Figure 1 shows the size of the outer box relative to the patient's head and the nasal passageways that represent the volume of primary interest. Figure 2 shows a view of the computational domain contained between the outer box and the patient's head. The volumetric computational grid is plotted onto the surface, and different grid densities can be appreciated in correspondence to face areas where the internal volumes belong to the nasal cavities, where most of the computational effort will be spent. The inner grid is further layered to better resolve the steep velocity gradients taking place in the proximity of the solid boundaries.

2.1 Details of the simulations

The simulations described below concern a steady inspiration forced by a pressure difference of $\Delta\overline{p} = 160Pa$ between the outer ambient and the nasopharynx, that corresponds to a state of breathing typical of a mild exercise [18]. Although the boundary conditions are stationary, an unsteady solver is used to compute up to 0.75 seconds of inspiration. The time step is 3×10^{-6} seconds. In what follows, results are presented for a laminar simulation, i.e. one where the Navier–Stokes equations are solved without a turbulence model, and

for a turbulent simulation where the Bousinnesq hypothesis of turbulent eddy viscosity ν_t and the $k-\omega-$SST model [11] is employed, based on solving additional PDEs for the turbulent kinetic energy k, and an additional, scale-setting turbulence variable ω that represents a specific dissipation rate. In its simplest form, the turbulent viscosity ν_t is simply given by $\nu_t = k/\omega$. Wall functions are used to avoid massive clustering of grid points near the walls. As previously stated, it is not our aim here to discuss the choice of the best mathematical and closure model for the flow, that is ongoing work.

A preliminary grid refinement study has been carried out, evaluating results obtained with meshes containing from 300,000 to 5M cells for both the laminar and the turbulent case. Although the less detailed mesh presented rather evident geometrical differences, including for example unrealistic representations of the volumes of the large sinuses, overall the global features of the flow field were always well predicted. As the two largest meshes (with 2.4M and 5M cells) yielded a flow rate that was unchanged within less than 0.1%, the remaining part of the computational study was carried out on the mesh with 2.4M cells.

In terms of computing time, the present computational experiments are rather small, with most of the cases run on a mesh size composed by 2.4M cells. We thus limit parallel computing to 4 cores for each case, and obtain a linear speedup. To compute 0.75s of steady inspiration about 4 days of wall clock time are needed, when using Intel Xeon CPUs at 3.16GHz. Thanks to the number of processors available, about the same time is required to complete the whole parametric study by running all the required cases in parallel. The computational cost of the turbulent case, owing to the additional differential equations, is about twice that of the laminar simulation. Depending upon the particular flow model adopted, the computational requirements are greatly varying. For example. a steady-state simulation would require far less computational resources, amounting to 2 hours on a laptop for the laminar case. A comparable wall clock time could be achieved for a single case by exploiting a larger number of CPUs.

3 Results

First an overall assessment of the results, corresponding to the flow field obtained with the laminar model, is provided. To begin with, figure 3 shows a three-dimensional, qualitative view of the computed solution, visualized in terms of its velocity field. The spatial rate of change of the velocity in the area of the turbinates can be appreciated thanks to the color and size of the arrows. The figure highlights the high velocity values reached in the downstream portion of the domain, owing to the gradually restricted cross-section.

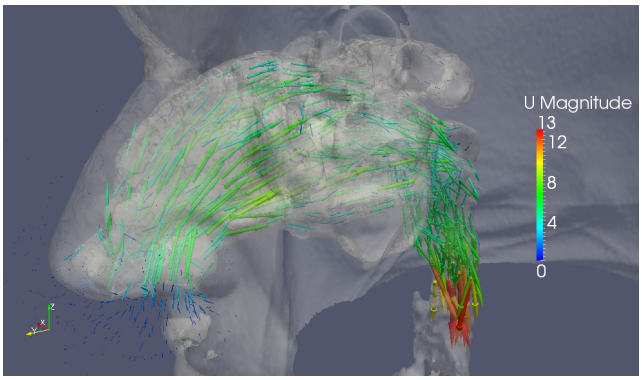

Fig. 3 Three-dimensional view of the nasal cavity flow corresponding to a steady inspiration. Arrows are oriented as the local velocity vector, with size and color determined from its modulus.

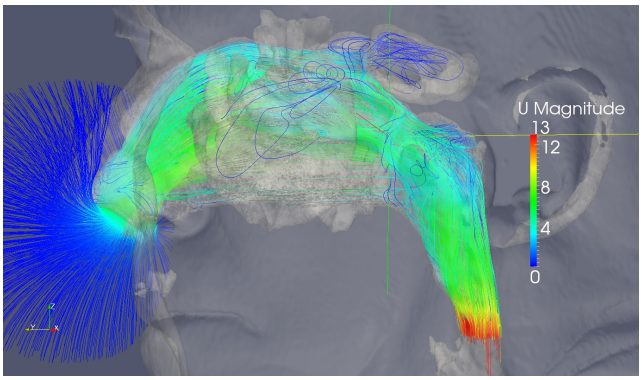

Fig. 4 Three-dimensional view of the nasal cavity flow corresponding to a steady inspiration. Flow is depicted here through the trajectory of massless lagrangian tracers, released in the region in front of the patient's head and color-coded with the local velocity.

Similarly, figure 4 shows the presence of a recirculating region in correspondence of the maxillary sinus, and – more importantly – on the uppermost region of the nasal cavity, at the upper boundary of the so-called olfactory cleft where most of the olfactory receptors are located.

Figure 5 is a sagittal slice of the flow field, corresponding to a location passing through the right passageway; the color map shows the modulus of velocity vector. The two images, corresponding to the very same location, compare the laminar (top) and the turbulent (bottom) simulations, and show that no large differences exist between the two.

The numeric values for the flow rate confirm what is already known from several previous studies, e.g. [8], i.e. the major role played by the middle meatus and, to a lower extent, by the inferior meatus in accounting for most of the flow rate.

A threshold value of radiodensity must be chosen to identify the geometric boundary of the volume of interest for the CFD analysis, in order to initiate the construction of a three-dimensional model by using edge detection image processing algorithms. Radiodensity is typically expressed in the Hounsfield unit (HU) scale, in which the radioden-

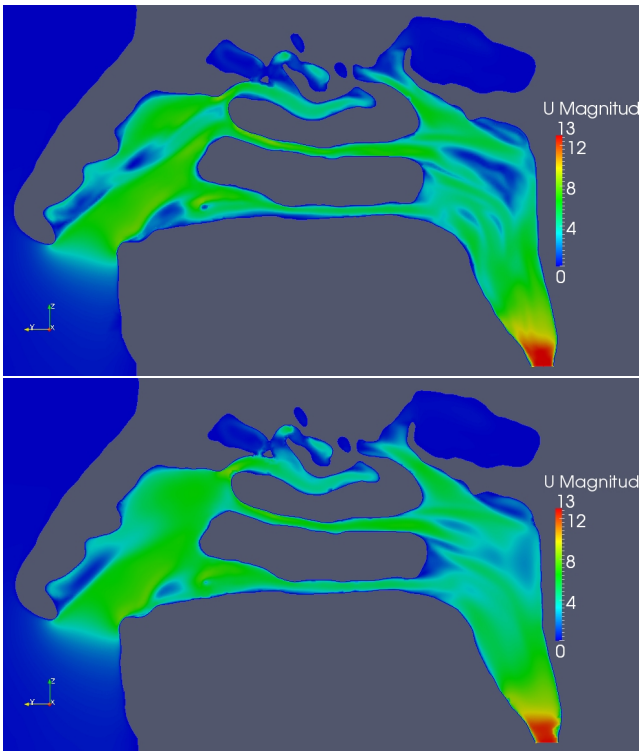

Fig. 5 Slice of the flow field with a sagittal plane that passes through the right passageway. Comparison between the laminar (top) and turbulent (bottom) solutions in terms of the modulus of the velocity vector.

HU	left nostril	right nostril	inferior turb.	middle turb.	superior turb.
-120	0.6495	0.7246	0.4344	0.5031	0.4352
-160	0.6007	0.6928	0.3976	0.4973	0.3972
-200	0.5926	0.6555	0.3940	0.4784	0.3745
-220	0.5594	0.6317	0.3776	0.4872	0.3247
-230	0.5645	0.6309	0.3973	0.4789	0.3179
-230LQ	0.5510	0.6440	0.3870	0.4970	0.3100
-240	0.5514	0.6308	0.3917	0.4815	0.3076
-280	0.5193	0.5876	0.3863	0.4558	0.2639

Table 1 Effects of the radiodensity threshold (expressed in HU units) on the observed flow rate (expressed in liters per second) in a coronal section. Selected regions of the nasal cavity are considered.

sity of distilled water at standard pressure and temperature is defined as zero HU, while the radiodensity of air is defined as -1000 HU. Thus, a change of one Hounsfield unit represents a change of 0.1% of the attenuation coefficient of water since the attenuation coefficient of air is nearly zero. For reference, fat is around -100 HU, muscles are 40 HU, and bones from 300 HU up.

To assess the importance of the choice of the radiodensity threshold, we have carried out a series of CFD simulations where the threshold is systematically varied. In this section, we only consider laminar simulations. With the flow being always driven by the same pressure difference between the outer ambient and the throat, measuring the flow

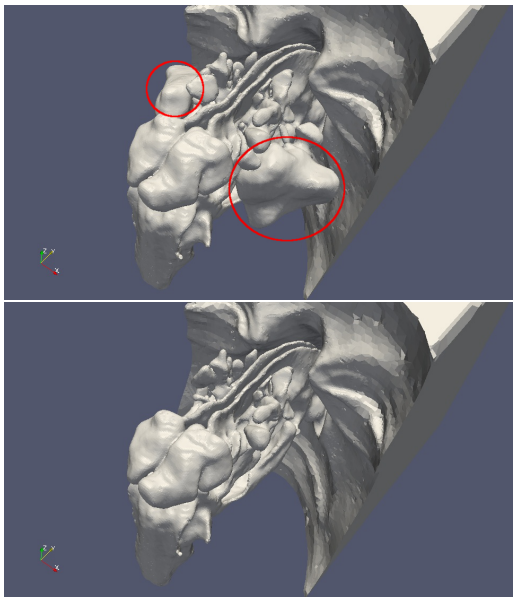

Fig. 6 Effect of the radiodensity threshold on the reconstructed geometry. By going from -200 HU (top) to -280 HU (bottom), the internal volume becomes progressively reduced, and several volume fractions related to large sinuses (circled in top figure) are excluded.

rate through the nostrils gives an indication of the global sensitivity of the CFD results to the segmentation threshold. Table 1 reports the values, expressed in liters per second, of the observed flow rate in selected regions of the flow field, as a function of the segmentation threshold expressed in HU. The threshold is varied around the empirically determined best value of -230 HU. Two extreme cases, with the threshold set very low at -120 HU and very high at -280 HU are also considered. These extremal cases are way beyond what an experienced user could select, as exemplified in figure 6 where too high a threshold is shown to remove large portions of the reconstructed volume.

Figure 7 quantifies how the flow rate changes with the chosen threshold. The flow rate is evaluated in a separate manner for the left and right nostril, as well as for the regions of the three turbinates. The nearly monotonic behavior of the data is consistent with the reconstructed volume increasing by increasing the threshold: as the flow is driven by a fixed pressure difference, a larger volume, with a larger cross-section at the inlet, implies a larger flow rate.

A visual inspection of the impact of changing the HU threshold on the flow field is given in figure 8, that shows a color map for the horizontal velocity component (positive from right to left).

The CT scan we employed has an axial resolution of 0.625mm. We had the same scan reconstructed at a lower axial resolution of 1.25mm, so that the results for an otherwise identical procedure can be meaningfully compared. In Table 1, the lower-quality mesh reconstructed for -230 HU is denoted with LQ.

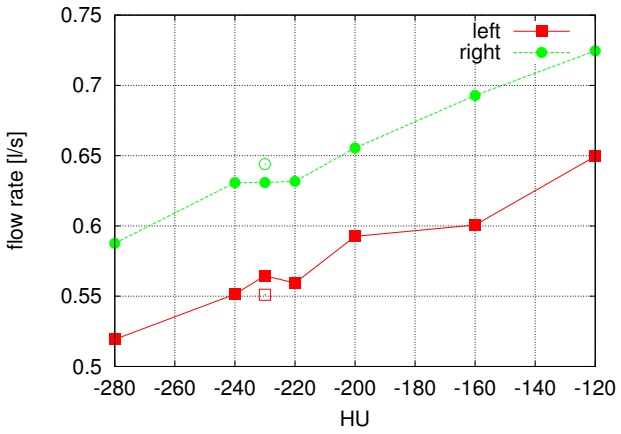

Fig. 7 Flow rate (expressed in liters per second) through the right (green curve, circles) and left (red curve, squares) nostrils, as a function of the radiodensity threshold (expressed in HU) employed for the reconstruction of the three-dimensional volume of interest. The plateau between -240 and -220 HU can be appreciated. The open symbols are for the low-quality reconstruction at -230 HU (see text).

4 Discussion

Our procedure for setting up the numerical simulation from a patient's CT scan, although still rather young, is already demonstrating a remarkable efficiency in terms of operator time. In particular the step of building the mesh where the equations of motion are discretized and solved, which is essential in determining the quality of the final results, can be designed once and for all by tuning the parameters of the `snappyhexmesh` program, and after that requires almost no operator time. We also regard our choice of employing a computational domain which entirely surrounds the patient's head as particularly rewarding. A crude estimate of the computational overhead related to solving the fluid equations in the outer region is a significant 40% of the overall computational cost. However, we consider this a fair price to be paid for rendering the simulation free from an unacceptable source of arbitrariness. This aspect is bound to become far more important when the expiration phase of the respiratory cycle will be considered. Figures 3 and 4 highlight how near the nose tip a non-trivial velocity field is computed: this would be very difficult to be accounted for correctly, should the inlet boundary conditions be imposed straight at the nostrils. Moreover, the flow velocity outside the nasal cavity is negligibly small everywhere but in the immediate vicinities of the nostrils, lending support to the simple zero-gradient boundary condition employed there.

In terms of operator time, the only time-consuming part of the procedure is the segmentation of the CT image leading to the STL geometry, that requires 15–30 minutes. We regard this as a very positive result, since only a few years ago reducing such time down to a few days was described as an important advancement [23]. The cost of this part of

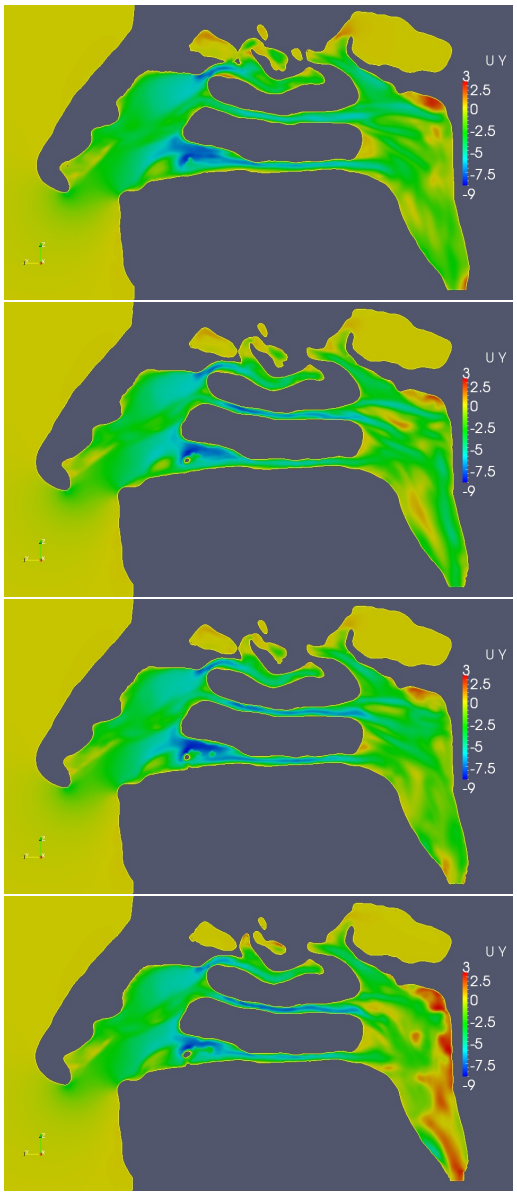

Fig. 8 Effect of the radiodensity threshold on the computed horizontal velocity field. From top to bottom: threshold at -120 HU, -220 HU, -230 HU, -280 HU. Positive velocity is from right to left.

the procedure in terms of operator time is clearly very important as it impacts the ability of such a procedure to be deployed in daily clinical use. Significantly changing the value of the threshold introduces evident visual effects in the reconstructed volume. In general increasing the threshold value implies that the selected volume within the nasal cavity decreases; at some point the large sinuses, which communicate with the main ducts through relatively small orifices, the ostii, become excluded from the volume of interest, as shown in figure 6.

The availability of the full velocity field allows the identification of its main features, and a thourough examination of their functional significance. For example, from figure 4

the sophisticated fluid dynamical design of the nasal cavities can be appreciated: generally disadvantageous recirculation regions are present only where a longer residence time becomes advantageous for the hodorant molecules to impress the olfactory receptors more effectively. However, owing of the lack of true *in vivo* validation, such results should always be critically considered. For example, even though the majority of the available CFD results are computed with turbulence models, figure 5 shows little or no difference between laminar and turbulent simulations, suggesting that, at this flow rate, the nasal flow is hardly turbulent in most of the volume, although it is clearly massively separated (in the available literature, the different notions of turbulent flow and of unsteady separated flow are sometimes confused). On closer scrutiny, one notices that the top plot of figure 5 presents a tendency towards stronger recirculating and separated regions. This is easily explained by the regularizing effect of turbulent viscosity in the turbulent simulation. The specific flow model did not produce a significant effect on the global value of the flow rate, which is found to differ by less than 1% between the laminar and turbulent simulations, further indicating that the majority of the flow develops in the laminar regime.

In terms of quantitative results, the parametric study presented here explicitly addresses for the first time the sensitivity of the solution (or, at least, of some global characteristics of the solution) upon the segmentation threshold. It is interesting to note that our results (cfr. table 1 and figure 7) support, for both nostrils, the existence of a plateau between -240 and -220 HU where the flow rate presents minimal changes. This is precisely where visual inspection suggests the geometric reconstruction to be most accurate. Moreover, it can be appreciated how only the extreme values of threshold produce reconstructed volumes with significant differences. However, even in these cases the flow field does not show evident misrepresentations, and the computed global quantities present only modest variations. Overall, most of the changes in a global quantity like the flow rate can be simply ascribed to the change in volume, with the inner velocity field being only marginally affected by the geometric changes.

The comparison of the flow rate in the right and left passageways, as well as the partial flow rate in the inferior, medium and superior turbinate, show that halving the axial resolution of the CT scan affects a global result like the flow rate by a change of the order of 1%. This can be appreciated by looking again at figure 7, where the points from the lower-resolution reconstruction are indicated with open symbols. Overall, these changes are entirely in line with the small changes that are introduced by the unavoidable uncertainty in the segmentation levels. However, there is an indication that, owing to the complex three-dimensional geometry of the nasal cavity, it would be desirable to employ a CT scan with as isotropic a spatial resolution as possible.

5 Conclusions

In this work we have described a preliminary, yet essential step towards making CFD analysis of the nasal passageways an useful tool in the daily ENT practice. Two issues are discussed: how the quantitative outcome of the CFD analysis depends upon the quality of the available CT scan, and how the choice for a radiodensity threshold impacts the accuracy of the reconstructed nasal cavity and, as a consequence, the computed flow field. Our results indicate that a standard, well carried out CT scan should be enough to produce robust results. On the other hand, the choice of the radiodensity threshold may become a critical issue, since global features of the flow like the mass flow rate show a non-negligible dependence upon this parameter. However, most of this dependence can simply be ascribed to the volumetric changes of the considered geometry, with the inner flow field being only marginally affected. Moreover, we have found that, when the threshold is set by the operator in such a way that the reconstruction presents reasonable details from an anatomical standpoint, a plateau does exist where even the global flow rate depends weakly, if at all, on the segmentation threshold.

Of course, it remains to be assessed whether and how this relative robustness of the CFD procedure, demonstrated here for global quantities like the flow rate, applies to the fine-scale details of the flow. This is a necessary and future step that can be meaningfully carried out once a particular mathematical and physical model (e.g. Large Eddy Simulation vs Reynolds–Averaged Navier–Stokes equations) and a specific turbulence model are chosen. Thus the results obtained so far are not yet conclusive in this respect, but do allow for an optimistic outlook.

Acknowledgements Part of the calculations presented here have been carried out on the Lagrange supercomputer of the CINECA (formerly CILEA) computing center in Milano / Bologna, Italy. We thankfully acknowledge their support.

References

1. Arbour, P., Bilgen, E., Girardin, M.: Experimental study of nasal velocity fields in a human nasal fossa by laser anemometry. Rhinology **23**, 201–207 (1985)
2. Chen, X., Lee, H., Chong, V., Wang, D.: Assessment of septal deviation effects on nasal air flow: a computational fluid dynamics model. American Laryngological Rhinological and Otological Society **119**, 1730–1736 (2009)
3. Doorly, D., Taylor, D., Gambaruto, A., Schroter, R., Tolley, N.: Nasal architecture: form and flow. Philosophical Transaction of the Royal Society **366**, 3225–3246 (2008)

4. Elad, D., Liebenthal, R., Wenig, B., Einag, S.: Analysis of air flow pattern in the human nose. Med Bio Eng Comput **31**, 585–592 (1993)
5. Fedorov, A., Beichel, R., Kalpathy-Cramer, J., Finet, J., Fillion-Robin, J.C., Pujol, S., Bauer, C., Jennings, D., Fennessy, F., Sonka, M., Buatti, J., Aylward, S., Miller, J., Pieper, S., Kikinis, R.: 3D Slicer as an Image Computing Platform for the Quantitative Imaging Network. Magnetic Resonance Imaging p. 22770690 (2012). Http://www.arxiv.org
6. Hahn, I., Scherer, P., Mozell, M.: Velocity profiles measured for airflow through a large-scale model of the human nasal cavity. J. Appl. Physiol. **75**, 2273–2287 (1993)
7. Hoerschler, I., Schoroeder, W., Meinke, M.: On the assumption of steadiness of nasal cavity flow. Biomechanics **43**, 1081–1085 (2010)
8. Kleinstreuer, C., Zhang, Z.: Airflow and particle transport in the human respiratory system. Ann. Rev. Fluid Mech. **42**, 301–334 (2010)
9. Leong, S., Chen, X., Lee, H., Wang, D.: A review of the implications of computational fluid dynamic studies on nasal airflow and physiology. J. of Rhinology **48**, 139–145 (2010)
10. Martonen, T., Quan, L., Zhang, Z., Musante, C.: Flow simulation in the human upper respiratory tract. Cell Biochem Biophys **37**, 2736 (2002)
11. Menter, F.: Two-Equation Eddy-Viscosity Turbulence Models for Engineering Applications. AIAA J. **32**(8), 1598–1605 (1994)
12. Nathan, A., Eccles, R., Howarth, P., Steinsvag, S., Togias, A.: Objective monitoring of nasal patency and nasal physiology in rhinitis. J Allergy Clin Immunol **115**(3), S442–S459 (2005)
13. Pope, S.: Turbulent Flows. Cambridge University Press, Cambridge (2000)
14. Quadrio, M., Pipolo, C., Corti, S., Lenzi, R., Messina, F., Pesci, C., Felisati, G.: Review of computational fluid dynamics in the assessment of nasal air flow and analysis of its limitations. Eur Arch Otorhinolaryngol (2013). DOI 10.1007/s00405-013-2742-3
15. Rhee, J., Pawar, S., Garcia, G., Kimbell, J.: Toward Personalized Nasal Surgery Using Computational Fluid Dynamics. Arch Facial Plast Surg pp. E1–E6 (2011)
16. Schumacher, M.: Nasal dyspnea: the place of rhinomanometry in its objective assessment. Am. J. Rhinol. **18**(1), 41–6 (2004)
17. Stewart, M., Ferguson, B., Fromer, L.: Epidemiology and burden of nasal congestion. Int. J. General Medicine **3**, 37–45 (2010)
18. Wang, D., Lee, H., Gordon, R.: Impacts of Fluid Dynamics Simulation in Study of Nasal Airflow Physiology and Pathophysiology in Realistic Human Three-Dimensional Nose Models. Clinical and Experimental Otorhinolaryngology **5**(4), 181–187 (2012)
19. Weller, H., Tabor, G., Jasak, H., Fureby, C.: A Tensorial Approach to Computational Continuum Mechanics using Object-Oriented Techniques,. Computers in Physics **12**, 620–631 (1998)
20. Xiong, G., Zhan, J., Zuo, K., Li, J., Rong, L., Xu, G.: Numerical flow simulation in the post-endoscopic sinus surgery nasal cavity. Med Bio Eng Comput **46**, 1161–1167 (2008)
21. Zhao, K., Blacker, K., Luo, Y., Bryant, B., Jiang, J.: Perceiving nasal patency through mucosal cooling rather than air temperature or nasal resistance. PLoS ONE **6**(10), e24,618 (2011)
22. Zhao, K., Dalton, P., Yang, G., Scherer, P.: Numerical modeling of turbulent and laminar airflow and odorant transport during sniffing in the human and rat nose. Chem. Senses **31**, 107–118 (2006)
23. Zhao, K., Scherer, P., Hajiloo, S., Dalton, P.: Effect of anatomy on human nasal air flow and odorant transport patterns: implications for olfaction. Chem. Senses **29**, 365–379 (2004)
24. Zhu, J., Lim, K., Thong, K., Wang, D., Lee, H.: Assessment of airflow ventilation in human nasal cavity and maxillary sinus before and after targeted sinonasal surgery: A numerical case study. Respiratory Physiology & Neurobiology **194**, 29–36 (2014)